Nanoscale

Apex Hydrogen Bonds in Dendron Assembly Modulate Close-packed Mesocrystal Structures

Journal:	*Nanoscale*
Manuscript ID	NR-ART-10-2022-005458.R1
Article Type:	Paper
Date Submitted by the Author:	31-Oct-2022
Complete List of Authors:	Jun, Taesuk; Yonsei University, Chemical and Biomolecular Engineering Park, Hyunjun; Yonsei University, Chemistry Jeon, Seungbae; Yonsei University, Chemical and Biomolecular Engineering Ahn, Hyungju; Pohang Accelerator Laboratory, Industry Technology Convergence Centre Jang, Woo-Dong; Yonsei University, Chemistry Lee, Byeongdu; Argonne National Laboratory, Advanced Photon Source Ryu, Du Yeol; Yonsei University, Chemical and Biomolecular Engineering

ARTICLE

Apex Hydrogen Bonds in Dendron Assembly Modulate Close-packed Mesocrystal Structures

Received 00th XXX 20xx,
Accepted 00th XXX 20xx

DOI: 10.1039/x0xx00000x

Taesuk Jun,[a] Hyunjun Park,[b] Seungbae Jeon,[a] Hyungju Ahn,[c] Woo-Dong Jang,[b,*] Byeongdu Lee,[d,*] and Du Yeol Ryu[a,*]

The close-packed mesocrystal structures from soft-matter assemblies have recently received attention due to their structural similarity to atomic crystals, displaying the various sphere-packing Frank-Kasper (FK) and quasicrystal structures. Herein, the diverse mesocrystal structures are explored in the second-generation dendrons (G2-X) designed with the identical wedges, in which the terminal functionalities X = $CONH_2$ and CH_2NH_2 represent two levels of the strong and weak hydrogen-bonding apexes, respectively. The cohesive interactions at the core apex, referred to as the core interactions, are effectively modulated by forming the heterogeneous hydrogen bonds between these two functional units. For the dendron assemblies compositionally close to each pure component of G2-$CONH_2$ and G2-CH_2NH_2, their own FK A15 and C14 phases dominate over other phases, respectively. We manifest the existence of the wide-range FK σ including dodecagonal quasicrystal (DDQC) phases from the dendron mixtures between G2-$CONH_2$ and G2-CH_2NH_2, providing an experimental phase sequence of A15–σ–DDQC–C14 as the core interactions are alleviated. Intriguingly, the temperature dependence of particle sizes shows that the high plateau values of particle sizes maintain equivalent until each threshold temperature (T_{th}), followed by the prompt decrease above the T_{th}. A decrease in T_{th} by alleviating the core interactions and its composition dependence suggest that the more size-disperse particles, the more susceptible to the chain exchange with increasing temperature. Our results on the formation of supramolecular dendron assemblies provide a guide to understand the core-interaction dependent mesocrystal structures toward the fundamental principle underlying the temperature dependence of their particle sizes.

Introduction

Most of the metallic elements usually pack together into simple high-symmetry structures, like body-centred cubic (BCC), face-centred cubic, and hexagonal close-packed phases,[1-3] except for a few complex structures in manganese and uranium.[4-6] In contrast, the soft-matter spheres obtained from the single-component molecular assemblies have recently emerged as the synthetic building units prone to transform into complex close-packed mesocrystal structures, where the spherical particles with different sizes and shapes pack into low-symmetry structures.[7-9] These point-like particle assemblies are analogous to these of metal alloys in three-dimensional (3D) packing characteristics such as the coordination number (CN), particle size and shape dispersity.[10,11] The low-symmetry phases observed in soft-matter assemblies include Frank-Kasper (FK) structures[12-15] as well as 10- and 12-fold quasiperiodic lattices.[16-19] To date, these sophisticated mesocrystal structures have been identified in the molecular self-assembly of dendritic molecules,[12,20-22] surfactants,[9,15] block copolymers,[14,23] amphiphiles,[24,25] and other soft matters.[26-28] Some of these unconventional structures have been found to possess the unique properties applicable for photonic and electronic devices.[29,30]

In order to infer the assembling principle of molecules into thermodynamically stable structures, it is essential to understand the formation of complex phases and their packing mechanism. Thermotropic and lyotropic liquid crystals (LCs) are found beneficial to address such challenges because their modular features can afford to provoke the packing diversity arising from the delicate thermodynamic balance in such systems.[31] In particular, the dendron assembly is a simple and versatile platform that has provided a rich series of 2D columnar and 3D sphere-packing structures,[32,33] in which the cohesive interactions at the core apex, referred to as the core interactions, are the attractive force acting radially towards the body and peripheral chains.[21,25,34-36] Their supramolecular assemblies associated with unique architectures have enabled earlier access to the observation of well-defined mesocrystal structures such as the FK and quasicrystal phases.[12,20,22,37]

The pioneering studies by Percec, Ungar, and coworkers well demonstrated the FK A15 and σ phases and dodecagonal quasicrystal (DDQC) phase demonstrated by adjusting the dendron's structural combination and generation number.[12,20-22,34,38] By presenting the radial distribution of volume functions (dV/dr) for the sphere-packing structures, they suggested that the dendritic wedges determine the geometry of particle assemblies.[12,13,39] In this concept of topologically close-packed structures, the body-periphery composition in dendron architectures influences the mesoscale packing structures of dendritic assemblies.[35,40-42] Furthermore, it has been believed that the cohesive interactions from the apex functional units also play

[a]*Department of Chemical and Biomolecular Engineering, Yonsei University, 50 Yonsei-ro, Seodaemun-gu, Seoul 03722, Korea.* E-mail: dyryu@yonsei.ac.kr
[b]*Department of Chemistry, Yonsei University, 50 Yonsei-ro, Seodaemun-gu, Seoul 03722, Korea.* E-mail: wdjang@yonsei.ac.kr
[c]*Industry Technology Convergence Centre, Pohang Accelerator Laboratory, 80 Jigok-ro, Nam-gu, Pohang 37673, Korea.* E-mail: blee@anl.gov
[d]*Advanced Photon Source, Argonne National Laboratory, Argonne, IL 60439, USA.*
†Electronic Supplementary Information (ESI) available: See DOI: **https://doi.org/10.1039/x0xx00000x**

an important role in guiding specific packing structures. Our previous study highlighted that the discrete increase in the core interactions on the single-component dendron assemblies resulted in a remarkable increase in the dendron's interfacial tension (γ_o) between alkyl chains (corona) and benzyl ether bodies (core).[43] The thermotropic and lyotropic approaches to the apex-dependent second-generation (G2) dendrons led to the observation of columnar and various mesocrystal structures. This finding triggered an interesting question as to how delicate control of the core interactions can affect diverse supramolecular assemblies, transitions, and the temperature dependence of particle sizes.

To answer this question, we explored the core-interaction dependent mesocrystal structures with two types of G2 dendrons, G2-$CONH_2$ and G2-CH_2NH_2, which represent two levels of the strong and weak hydrogen-bonding apexes, respectively. The core interactions were effectively modulated by forming the heterogeneous hydrogen bonds between these two apex units. In the dendron assemblies compositionally close to each pure component of G2-$CONH_2$ and G2-CH_2NH_2, their own FK A15 and C14 phases dominated over other phases, respectively. However, the FK σ phase including DDQC phase widely existed over the composition of the dendron mixtures, providing an experimental phase sequence of A15–σ–DDQC–C14 by alleviating the core interactions. From the temperature dependence of particle sizes, we generalized that the high plateau values of particle sizes maintain equivalent until each threshold temperature (T_{th}), followed by the prompt decrease above the T_{th}. Our concept of a master curve for T_{th} pointed out the size dispersity effect induced by the core-interaction dependent mesocrystal structures.

Experimental

Synthesis and chemical characterisation

All reagent-grade chemicals were purchased from Sigma-Aldrich, TCI, Alfa Aesar, Duksan, or Fluka. The commercial products, dichloromethane (CH_2Cl_2), *n*-hexane, tetrahydrofuran (THF), and methanol (CH_3OH) were freshly distilled before each use, and all other chemicals were used as received without further purification. To characterise the molecular structures, ^1H and ^{13}C NMR spectra were measured by DPX 400 (Bruker) at room temperature in deuterated CH_2Cl_2 (CD_2Cl_2) and chloroform solutions, respectively. Matrix-assisted laser desorption ionisation time-of-flight mass spectrometry (MALDI-TOF-MS) was operated with LRF20 (Bruker) using dithranol (1,8,9-trihydroxyanthracene) as a matrix. Detailed information on the synthetic processes was described in the previous study.[43] The bulk densities of the dendrons were evaluated using a solution mixture of water and ethanol once the sample species were constantly suspended in the solution for 30 min. The thermal properties of all samples were characterised by a Perkin-Elmer Diamond differential scanning calorimetry (DSC) with loading amounts of approximately 10 mg under nitrogen flow. The temperature and heat flow scales were calibrated using indium as the standard material.

Small-angle X-ray scattering (SAXS) measurements

SAXS experiments were performed at the 4C and 9A beamlines of the Pohang Accelerator Laboratory, Korea or the 12-ID-B beamline of Advanced Photon Source, US. The operating conditions for the 4C and 9A beamlines were set at a wavelength of λ = 0.633 Å, the sample-to-detector distance (SDD) of 1 m, and exposure time of 1 – 15 s; these were similarly set at the 12-ID-B beamline with λ = 0.954 Å, SDD = 2 m, and exposure time of 1 – 10 s. The scattered intensities were collected on 2D detectors (Rayonix SX165 and Pilatus2M) at the target temperatures. The system temperature was selected as the mean value during heating at a rate of 1.0 °C/min under nitrogen flow.

Electron density (ED) map reconstructions

The SAXS intensity profiles of all dendron assemblies were recorded to render the ED maps of each characteristic sphere-packing phase. Using MATLAB, the structure-factor intensities and positions for each peak over q = 0.1 – 5.0 nm^{-1} were assigned according to each space-group symmetry and lattice parameter,[44,45] then recorded as the input values for SUPERFLIP.[46] Random phases were initially generated through a charge-flipping algorithm of SUPERFLIP, and the densities at each pixel in a unit cell were examined. If the calculated density is below zero (indicating an unphysical result), it is multiplied by -1 to render it positive. A discrete Fourier transform of the resulting density maps was employed to regenerate new structural factors, which were again subjected to other iterations. The converged results were averaged and visualised using the MATLAB software (in 90% contour levels) to construct Voronoi cells for the experimental polyhedrons.

Results and discussion

Fig. 1a illustrates the chemical structures of (3,4,5-3,5)12G2-X dendrons with two different terminal units, X = $CONH_2$ and CH_2NH_2 at the same body and peripheral chains, where the two functionalities represent the strong and weak hydrogen-bonding apexes, respectively.[43] If the G2 dendron analogues possessing the identical wedge are miscible, a heterogeneous hydrogen bond can be formed between these two apex units. As an easy access to controlling the supramolecular sphere-packing structures, this chemical compatibility is essentially required for modulating the core interactions that attract the wedges.

The dendron mixtures between G2-$CONH_2$ and G2-CH_2NH_2 were prepared by a solvent casting from a co-solvent of chloroform and subsequently dried under vacuum before thermal treatments. DSC measurements were conducted at heating/cooling rates of ± 10 °C/min between -30 and 150 °C to trace the phase behaviours of the dendron assemblies (Fig. 1b and S1). The large endotherms and exotherms at lower temperatures upon heating and cooling, respectively, imply that the peripheral alkyl chains melt below room temperature, and the second endotherms (or exotherms upon cooling) at higher temperatures represent each clearing temperature of LC phases into an isotropic state (T_{iso}).

As the mass fraction (f) of G2-CH_2NH_2 increases, the magnitude of the enthalpy change ($|\Delta H|_{iso}$) at isotropisation and the T_{iso} decreases (Fig. 1c). Above all, there are no indications of macrophase separation that would generate two separate transitions in the immiscible binary mixtures. In this framework of the dendron assemblies arising from the heterogeneous hydrogen bonds between two apex units attached to the identical wedge, $|\Delta H|_{iso}$ can be an indicator of the dendron's overall interfacial tension (γ_o) that signifies the core interactions. Thus, we speculate that the consistent decreases in $|\Delta H|_{iso}$ and T_{iso} by compositionally increasing f are attributed to weakening the core interactions in the dendron assemblies. Even the values of $|\Delta H|$ at lower temperatures are found to be the same decreasing

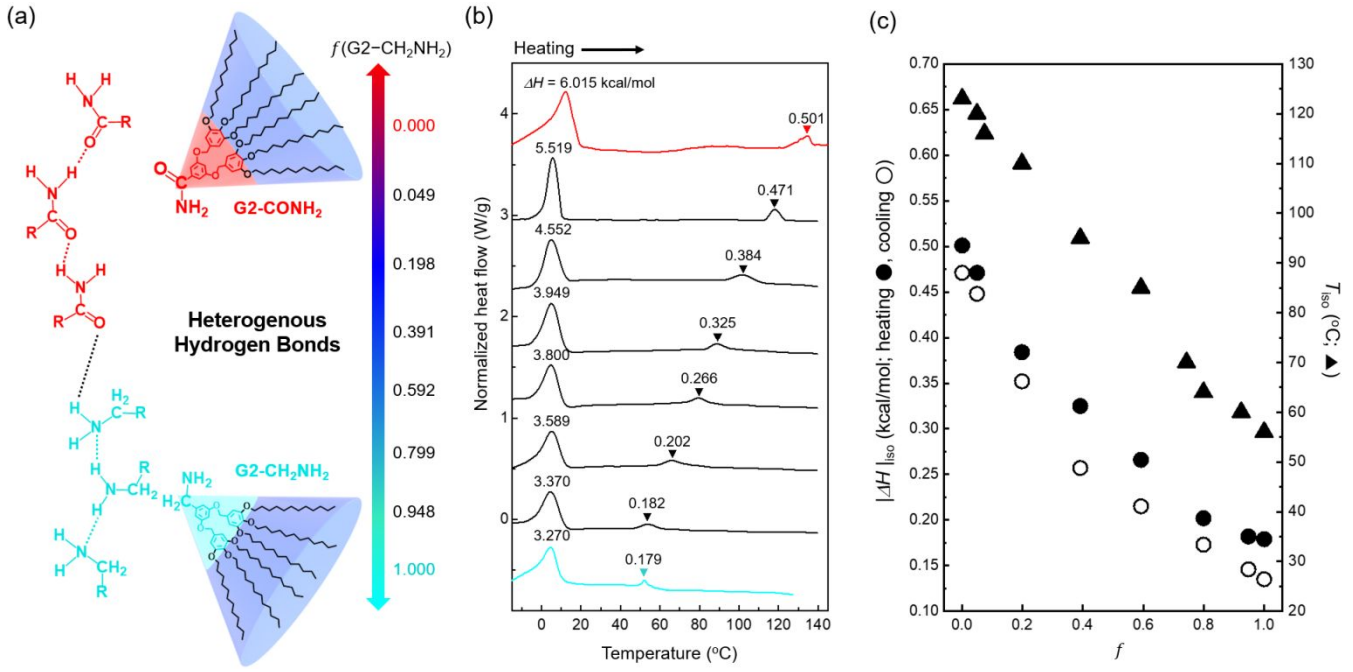

Fig. 1 (a) Chemical structures of G2 dendrons, (3,4,5-3,5)12G2-X with two different terminal units, X = $CONH_2$ and CH_2NH_2 at the same body and peripheral chains, in which the two functionalities represent the strong and weak hydrogen-bonding apexes, respectively. (b) DSC thermograms of the dendron assemblies, measured at a heating rate of 10 °C/min from -30 to 150 °C. The large endotherms at lower temperatures upon heating imply that the peripheral alkyl chains melt below room temperature, and the second endotherms represent each clearing temperature of LC phases into an isotropic state (T_{iso}). (c) $|\Delta H|_{iso}$ (open and closed circles) and T_{iso} (closed triangle) as a function of f.

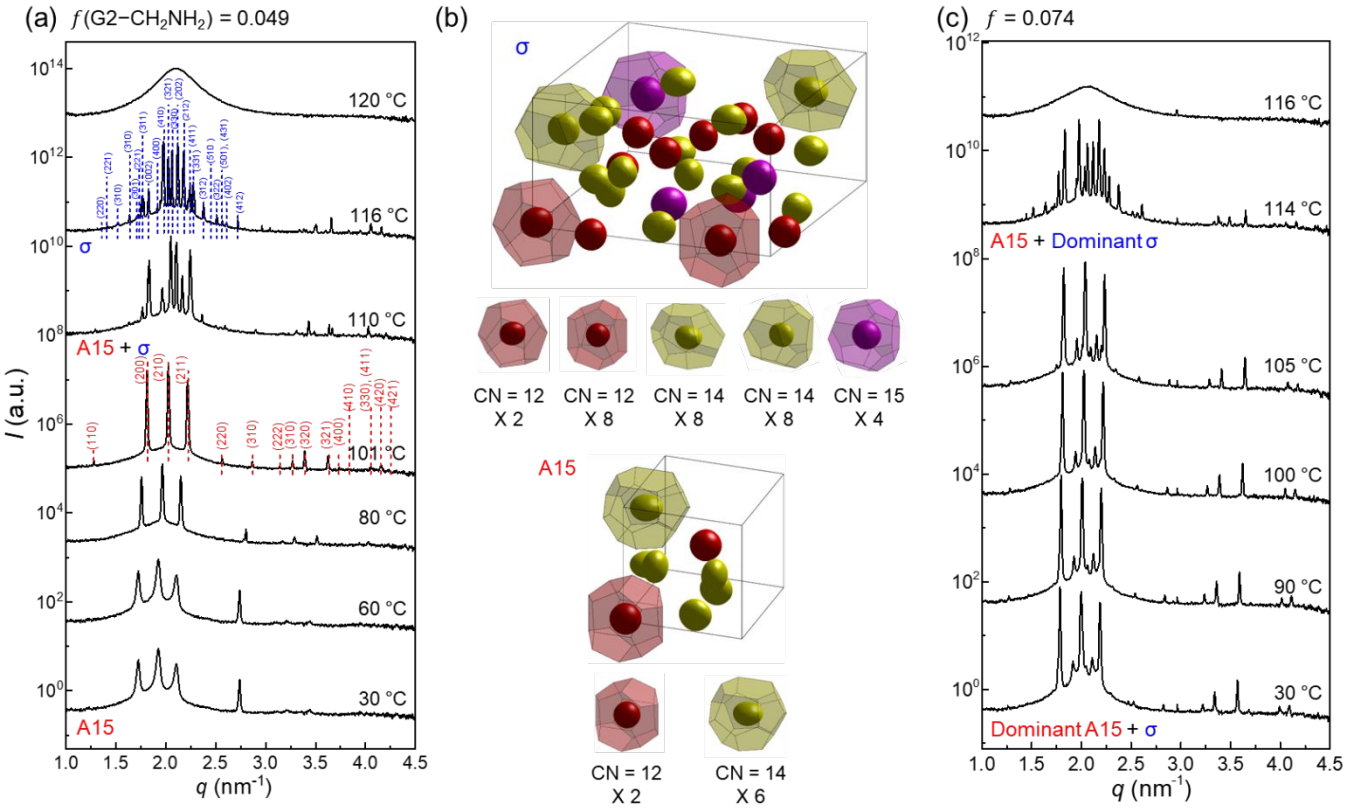

Fig. 2 (a) SAXS intensity profiles of a dendron assembly with f = 0.049. A cubic A15 phase measured at 30 °C becomes increasingly distinctive up to 101 °C, and reorganises to a tetragonal σ phase, then to an isotropic phase above 120 °C. (b) ED maps reconstructed from the X-ray scattering data, where the dendron cores are displayed in 90% contour levels (isosurfaces) and colour-coded with a sequence of red-yellow-magenta-cyan-blue according to each particle type for clarity. (c) SAXS intensity profiles of a dendron assembly with f = 0.074. The A15 and σ phases coexist at temperatures lower than 116 °C.

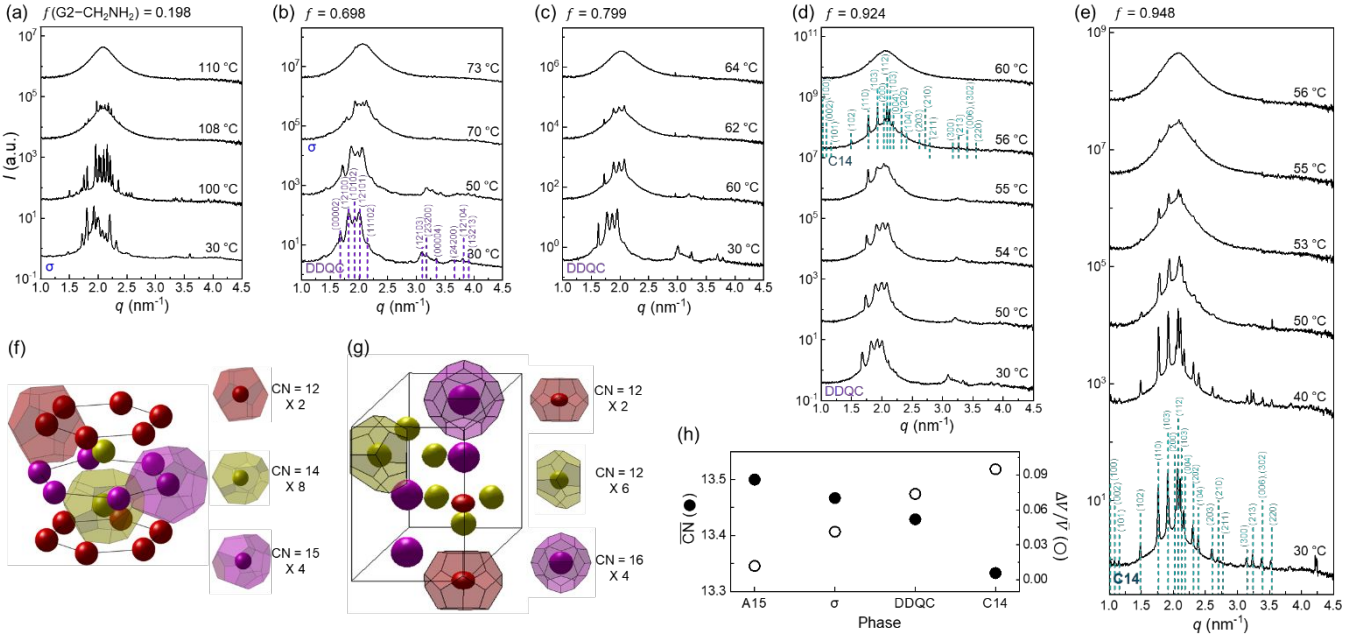

Fig. 3 SAXS intensity profiles of dendron assemblies with (a) f = 0.198 (only σ phase), (b) f = 0.698 (DDQC–σ transition), (c) f = 0.799 (only DDQC phase), (d) f = 0.924 (DDQC–C14 transition), and (e) f = 0.948 (only C14 phase). ED maps of (f) DDQC and (g) C14 phases obtained from dendron assemblies with f = 0.799 (c) and f = 0.948 (e) at 30 °C, respectively. For the ED map of DDQC phase, Voronoi cells are retrieved from its ideal fractional coordinates and the unit cell size determined from the X-ray data (Fig. S7). (h) $\overline{\mathrm{CN}}$ and $\Delta V/\overline{V}$ for the sphere-packing structures. Our experimental phase sequence of A15–σ–DDQC–C14 with increasing f follows an increase in $\Delta V/\overline{V}$ and a decrease in $\overline{\mathrm{CN}}$ as the core interactions are alleviated.

trend with $|\Delta H|_{\mathrm{iso}}$, indicating that the alkyl chain meltings are also affected by a gradual reduction of the core interactions. SAXS intensity profiles of all dendron assemblies were recorded for structural analysis at target temperatures, at which the constant interval of 5 min was applied to all samples during a stepwise heating process because of the relatively rapid kinetics in forming the mesocrystal structures. The scattering vector $q = (4\pi/\lambda)\sin\theta$, where 2θ and λ are the scattering angle and wavelength of the X-ray beam, respectively. To erase the previous thermal histories, the sample aggregates were first heated to 130 °C and cooled to room temperature at a rate of -10 °C/min. All samples were then annealed at 30 °C under vacuum, which is still higher than the crystallisation temperatures (5 ~ 12 °C) of the peripheral alkyl chains. Note that pure G2-$CONH_2$ exhibited hexagonal columnar (Col_h), A15, and BCC phases with increasing temperature.[43] At a small fraction of f = 0.049 (Fig. 2a), the SAXS profile measured at 30 °C shows a pattern corresponding to a cubic A15 phase, which becomes increasingly distinctive up to 101 °C, representing that a small amount of G2-CH_2NH_2 is sufficient to modify the packing structures manifested in pure G2-$CONH_2$. This cubic structure first reorganises to a tetragonal σ phase at the narrow temperature window of 110 to 116 °C, then to an isotropic phase above 120 °C. The A15–σ transition is accessed by a small alleviation of the core interactions; this type of transition was reported in a G3 dendron with a terminal COOH apex.[12]

Electron density (ED) maps were reconstructed from the X-ray scattering data using a SUPERFLIP software program.[44-46] The dendron cores are displayed in 90% contour levels (isosurfaces) and colour-coded with a sequence of red-yellow-magenta-cyan-blue according to each particle type for clarity, displaying that the larger particles (with higher CN) are, the more rounded in the cores. An A15 phase has two polyhedrons with CN = 14 and 12, whereas a σ phase has five different types of polyhedrons with CN = 15, 14, 14, 12, and 12 (Fig. 2b); these are, hereafter, all analyzed with the number of Voronoi cell, surface area, volume, and isoperimetric quotient (IQ), as listed in Table S1. At f = 0.074 (Fig. 2c), the A15 and σ phases coexist at temperatures lower than 116 °C. However, the σ phase continues to grow at the expense of the A15 phase as temperature increases, similarly observed at f = 0.103 (Fig. S2). In principle, this phenomenon indicates that increasing temperature in the system is consistent with a reduction of the hydrogen-bonding strength at the core apexes to produce more diverse particle species.

When increasing f to 0.198 (Fig. 3a), the A15 phase completely disappears and only the σ phase appears during the heating process before it becomes an isotropic phase at 110 °C. The σ phase window extends to f = 0.592 (Fig. S3), although the characteristic intensities of σ phase diminish with increasing f. At f = 0.698 (Fig. 3b), interestingly, the DDQC phase appears at 30 °C and retains the same structure up to 50 °C, which has three different types of polyhedrons with CN = 15, 14, and 12 (Fig. 3f), It further transforms into the σ phase at 70 °C. The weak intensity of σ phase is presumably attributable to smaller grain sizes prior to becoming an isotropic phase. The same trend continues to f = 0.743 (Fig. S4), although the DDQC–σ transition and isotropisation occur at slightly lower temperatures than those of f = 0.698. This type of DDQC–σ transition was also often observed in G3 dendrons with a terminal CH_2OH apex,[22] oligomeric G1 dendrons,[47] and AB_n dendron-like giant molecules[48].

The slow-cooling (-1 °C/min) phase from an isotropic state was not the DDQC but the σ phase within the experimental time scale of 1 day. However, the DDQC phase at f = 0.698 was fully recovered when the sample was reannealed at 30 °C for a long

period of 2 months, as shown by the 2D diffraction pattern and intensity profile of the DDQC phase (Fig. S5).

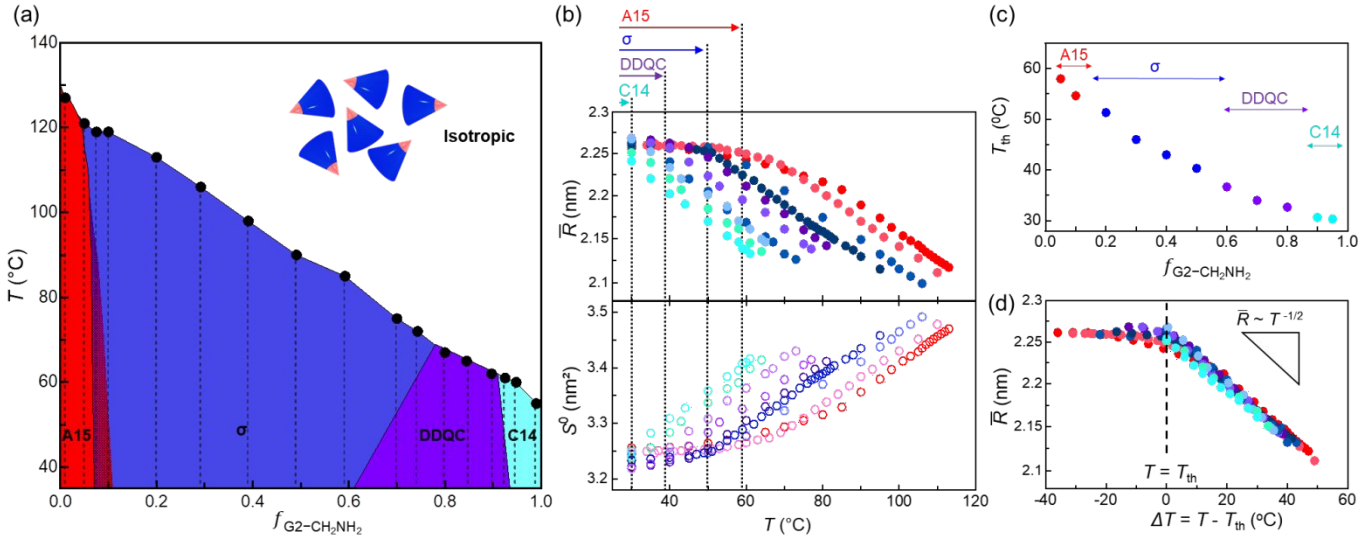

Fig. 4 (a) Phase diagram of temperature versus f, where the red, blue, purple, and cyan phase regions represent the A15, σ, DDQC, and C14 phases, respectively. The dashed lines denote the experimental traces, and the overlapped region between the A15 and σ phases represents a mixed phase between the two phases. (b) $\overline{R}$ and S^0 curves as a function of temperature. The symbols coloured in red, blue, purple, and cyan with increasing f denote the A15, σ, DDQC, and C14 phases, respectively. The dotted lines denote each T_{th}, which is the maximum temperature for keeping a consistent $\overline{R}$. (c) T_{th} as a function of f, which suggests that the more size-disperse particles, the more susceptible to the chain exchange with increasing temperature. (d) Master curve for $\overline{R}$ as a function of temperature, in which all the $\overline{R}$ curves are shifted and superimposed along the temperature axis onto a designated $f = 0.950$ with no T_{th}.

This evidence supports that the DDQC phase obtained from our dendron assemblies is an equilibrium state requiring long-time annealing, not a metastable state. For $f = 0.799$ (Fig. 3c), only the DDQC phase forms at 30 °C and becomes an isotropic phase at 64 °C, similar to those observed up to $f = 0.897$ (Fig. S6).

When the f approaches 0.924 (Fig. 3d), the DDQC phase formed at 30 °C undergoes a transition to the hexagonal C14 phase at 56 °C, which has three different types of polyhedrons with CN = 16, 12, and 12 (Fig. 3g), before becoming an isotropic phase at 60 °C. Notably, this unique DDQC–C14 transition is elicited by further alleviating the core interactions, which has never been reported to date. However, the dendron assembly at $f = 0.948$ (Fig. 3e) begins with a C14 phase at 30 °C and retains the same structure up to 55 °C prior to becoming an isotropic phase; this T_{iso} is slightly higher than that (50 °C) measured in pure G2-CH_2NH_2. In addition, the advent of the C14 phase only above $f = 0.924$ indicates that the delicate tuning of core interactions from the dendron mixtures meets the demanding condition for the rare C14 phase and its transition. It should be pointed out that the T_{iso} follows a decreasing tendency from 120 to 60 °C with increasing f because of the gradual reduction of the hydrogen-bonding strength at the core apex. Furthermore, all the LC transitions such as A15–σ, DDQC–σ, and DDQC–C14 were reproducible upon heating when the isotropic samples were annealed at 30 °C for a short period of 10 min.

Based on four experimental phases of A15, σ, DDQC, and C14 (Table S1) obtained at the specified temperatures, the dendron assemblies are treated as the Voronoi cells composed of polyhedrons. The average particle volume is set to $\overline{V} = 4\pi\overline{R}^3/3 = n^{-1}\sum_{i=1}^{n} V_i$, where $\overline{R}$ and V_i are the average spherical sizes of polyhedrons and the i^{th} polyhedron volume of n particles, respectively. We analyzed the average coordination number ($\overline{CN}$) and particle size dispersity ($\Delta V/\overline{V}$) depending on the sphere-packing structures (Fig. 3h). In principle, the more coordinated with the others, the less size-disperse the sphere-packing particles are, and vice versa.[49] Our experimental phase sequence of A15–σ–DDQC–C14 with increasing f follows an increase in $\Delta V/\overline{V}$ and a decrease in $\overline{CN}$ as the core interactions are alleviated. This suggests that the weak hydrogen-bonding dendrons are prone to make larger and smaller particles, whereas the strong hydrogen-bond dendrons favour more uniform-sized particles rather than larger and smaller ones, which is consistent with a theoretical consideration from the previous study.[43]

Fig. 4a summarises the overall phase diagram of temperature versus f, and the red, blue, purple, and cyan phase regions represent the A15, σ, DDQC, and C14 phases, respectively. It displays the composition-dependent phases of A15–σ–DDQC–C14 along with a linear decrease in T_{iso}. The σ and DDQC phases occupy 87.5% with respect to the entire range of f, representing that they accommodate the moderate and broad range of hydrogen-bonding strength at the core apex. For more details, we examined the temperature dependence of $\overline{R}$ and the interfacial area per chain ($S^0 = 4\pi\overline{R}^2/N_{agg}$), where N_{agg} denotes the aggregation number of average particles by $\overline{N}_{agg} = 4\pi\overline{R}^3 N_A\rho/3M$. Here, N_A, ρ, and M are the Avogadro's number, density, and the molecular weight of each dendron depending on f, respectively. Since the N_{agg} proportional to the average particle volume $\overline{R}^3$, S^0 is in turn inversely proportional to $\overline{R}$.

Fig. 4b shows the $\overline{R}$ and S^0 curves as a function of temperature. The symbols coloured in red, blue, purple, and cyan with increasing f denote the A15, σ, DDQC, and C14 phases, respectively. At lower temperatures, all the values remain relatively constant in each range of $2.24 < \overline{R} < 2.27$ nm and $3.22 < S^0 < 3.26$ nm². From the A15 to DDQC phases (the red to purple colours indicated on the top of Fig. 4b), the plateau $\overline{R}$ and S^0 values maintain equivalent until each threshold temperature (T_{th}), which is the maximum temperature for keeping a consistent $\overline{R}$. When temperatures further increase above the T_{th}, the $\overline{R}$

promptly decreases (S^0 increases) with the same slopes. Unlike the plateau $\overline{R}$ for the lower-f dendron assemblies close to the A15 phase, the $\overline{R}$ for the higher-f dendron assemblies close to the C14 phase immediately decreases (the S^0 increases) as soon as temperature increases.

A decrease in T_{th} by alleviating the core interactions and its composition dependence (Fig. 4c) suggest that the more size-disperse particles, along with the phase sequence of A15–σ–DDQC–C14, the more susceptible to the chain exchange with increasing temperature. Considering $\Delta T = T - T_{th}$, we constructed a master curve for $\overline{R}$ (Fig. 4d) as a function of temperature, where all the $\overline{R}$ curves are shifted and superimposed along the temperature axis onto a designated $f = 0.950$ with no T_{th}. Above each T_{th} of the sphere-packing structures, the $\overline{R}$ values follow a scaling relationship of $\overline{R} \sim T^{-1/2}$, indicating that the average particle sizes decrease with increasing temperature and the core-corona interfaces per chain become broader. As a consequence, our results on the temperature dependence of particle sizes establish an opportunity to associate the core-interaction dependent phases with their particle size dispersities.

As another aspect for the particle analysis, one can adopt the average radial distribution functions of volume (dV/dr) to explain dendritic particles as a function of radial distance (r) from the centre.[12,13,39] The dV/dr function with increasing temperature requires a higher dV/dr peak due to the lateral thermal expansion of peripheral chains and a shorter dV/dr tail due to the longitudinal contraction of the chains. This effect may bring about the less size-disperse phase at higher temperatures towards the uniform-sized structures like a BCC phase; this concept can be applied to the DDQC–σ transition measured in our study. However, the A15–σ and DDQC–C14 transitions, as observed in our study, represent that the particle size dispersity increases with increasing temperature; this is against the general explanation from the dV/dr for temperature-dependent particles.

Conclusion

We have demonstrated that the core-interaction dependent phases could be readily achieved by two homologous dendrons of G2-$CONH_2$ and G2-CH_2NH_2 possessing the different apexes but identical wedges. As the amount of weak hydrogen-bonding G2-CH_2NH_2 increases, the $|\Delta H|_{iso}$ and T_{iso} of the dendron assemblies gradually decrease, indicating that the heterogeneous hydrogen bonds between two apex units successfully tune the core interactions. In the dendron assemblies compositionally close to each pure component of G2-$CONH_2$ and G2-CH_2NH_2, their own FK A15 and C14 phases dominate over other phases, respectively. We manifest the existence of the wide-range FK σ phase including DDQC phase from the dendron mixtures, providing an experimental phase sequence of A15–σ–DDQC–C14 by alleviating the core interactions. Particularly, the DDQC–C14 transition elicited at $f = 0.924$ has never been accessed in the soft-matter assemblies to date. This phase sequence also corresponds to the increases in the particle size dispersity (or volume asymmetry).

The temperature dependence of $\overline{R}$ (and S^0) reveals that all the $\overline{R}$ curves are shifted and superimposed along the temperature axis onto a master curve for $\overline{R}$ with temperature, of which the T_{th} for keeping a consistent $\overline{R}$ decreases as the core interactions are alleviated. The stronger hydrogen-bonding dendrons with higher T_{th} favour more uniform-sized sphere-packing structures, whereas for the weaker hydrogen-bonding dendrons with lower or no T_{th}, the size-disperse particles are more susceptible to the chain exchange with increasing temperature, following the same phase sequence of A15–σ–DDQC–C14. Our thermotropic approach for supramolecular dendron assemblies offers valuable insight into the size dispersity effect induced by the core-interaction dependent mesocrystal structures. Moreover, our systematic concept based on controlling the hydrogen-bonding or cohesive interaction can be a simple strategy applicable for exploring the formation of a predictable, unidentified structure in supramolecular assemblies.

Author Contributions

T. J. performed SAXS and analyzed the properties of each Voronoi cell obtained from the reconstructed ED maps (under the instruction of D. Y. R. and B. L.). H. P. synthesised and characterised dendron samples using NMR spectroscopy and MALDI-TOF mass spectrometry (under the instruction of W. J.). S. J. assisted and reviewed the experimental results. H. A. assisted with the SAXS measurements and advised data analysis. D. Y. R., W. J., and B. L. discussed the results and wrote the manuscript. D.Y.R. and B. L. co-directed all aspects of the project.

Conflicts of interest

There are no conflicts of interest to declare.

Acknowledgements

We acknowledge the NRF Grants (2020R1A2C3004520, 2021R1A2C2006588, and 2022R1A4A1020543) funded by the Ministry of Science, ICT & Future Planning (MSIP), Korea. SAXS measurements were performed at Pohang Accelerator Laboratory (Korea) (4C and 9A beamlines) and Advanced Photon Source in the Argonne National Laboratory (U.S.) (12-ID-B beamline). The use of the APS is supported by the U.S. Department of Energy, Office of Basic Energy Sciences, under contract no. DE-AC0206CH11357.

References

1. H. L. Skriver, *Physical Review B*, 1985, **31**, 1909-1923.
2. P. Söderlind, O. Eriksson, B. Johansson, J. M. Wills and A. M. Boring, *Nature*, 1995, **374**, 524-525.
3. G. Grimvall, B. Magyari-Köpe, V. Ozoliņš and K. A. Persson, *Reviews of Modern Physics*, 2012, **84**, 945-986.
4. D. Hobbs, J. Hafner and D. Spišák, *Physical Review B*, 2003, **68**, 014407.
5. J. Hafner and D. Hobbs, *Physical Review B*, 2003, **68**, 014408.
6. A. C. Lawson, C. E. Olsen, J. W. Richardson, Jnr, M. H. Mueller and G. H. Lander, *Acta Crystallogr., Sect B: Struct. Sci.*, 1988, **44**, 89-96.
7. S. Lee, C. Leighton and F. S. Bates, *Proc. Natl. Acad. Sci.*, 2014, **111**, 17723-17731.
8. K. Yue, M. Huang, R. L. Marson, J. He, J. Huang, Z. Zhou, J. Wang, C. Liu, X. Yan, K. Wu, Z. Guo, H. Liu, W. Zhang, P. Ni, C. Wesdemiotis, W.-B. Zhang, S. C. Glotzer and S. Z. D. Cheng, *Proc. Natl. Acad. Sci.*, 2016, **113**, 14195-14200.
9. G. C. Shearman, A. I. I. Tyler, N. J. Brooks, R. H. Templer, O. Ces, R. V. Law and J. M. Seddon, *Liq. Cryst.*, 2010, **37**, 679-694.

10. N. Mott and H. Jones, *Journal*, 1936.
11. S. L. Altmann, *Band theory of metals: the elements*, Elsevier, 1970.
12. G. Ungar, Y. Liu, X. Zeng, V. Percec and W.-D. Cho, *Science*, 2003, **299**, 1208-1211.
13. G. Ungar and X. Zeng, *Soft Matter*, 2005, **1**, 95-106.
14. S. Lee, M. J. Bluemle and F. S. Bates, *Science*, 2010, **330**, 349-353.
15. S. A. Kim, K. J. Jeong, A. Yethiraj and M. K. Mahanthappa, *Proc. Natl. Acad. Sci.*, 2017, **114**, 4072-4077.
16. G. Ungar, V. Percec, X. B. Zeng and P. Leowanawat, *Isr. J. Chem.*, 2011, **51**, 1206-1215.
17. T. M. Gillard, S. Lee and F. S. Bates, *Proc. Natl. Acad. Sci.*, 2016, **113**, 5167-5172.
18. A. Jayaraman, C. M. Baez-Cotto, T. J. Mann and M. K. Mahanthappa, *Proc. Natl. Acad. Sci.*, 2021, **118**, e2101598118.
19. Y. Liu, T. Liu, X.-Y. Yan, Q.-Y. Guo, H. Lei, Z. Huang, R. Zhang, Y. Wang, J. Wang, F. Liu, F.-G. Bian, E. W. Meijer, T. Aida, M. Huang and S. Z. D. Cheng, *Proc. Natl. Acad. Sci.*, 2022, **119**, e2115304119.
20. V. S. K. Balagurusamy, G. Ungar, V. Percec and G. Johansson, *J. Am. Chem. Soc.*, 1997, **119**, 1539-1555.
21. V. Percec, C. H. Ahn, G. Ungar, D. J. P. Yeardley, M. Möller and S. S. Sheiko, *Nature*, 1998, **391**, 161-164.
22. X. Zeng, G. Ungar, Y. Liu, V. Percec, A. E. Dulcey and J. K. Hobbs, *Nature*, 2004, **428**, 157-160.
23. K. Kim, M. W. Schulze, A. Arora, R. M. Lewis, M. A. Hillmyer, K. D. Dorfman and F. S. Bates, *Science*, 2017, **356**, 520-523.
24. Z. Su, C.-H. Hsu, Z. Gong, X. Feng, J. Huang, R. Zhang, Y. Wang, J. Mao, C. Wesdemiotis, T. Li, S. Seifert, W. Zhang, T. Aida, M. Huang and S. Z. D. Cheng, *Nat. Chem.*, 2019, **11**, 899-905.
25. Y. Liu, T. Liu, X.-y. Yan, Q.-Y. Guo, J. Wang, R. Zhang, S. Zhang, Z. Su, J. Huang, G.-X. Liu, W. Zhang, W. Zhang, T. Aida, K. Yue, M. Huang and S. Z. D. Cheng, *Giant*, 2020, **4**, 100031.
26. M. Huang, C.-H. Hsu, J. Wang, S. Mei, X. Dong, Y. Li, M. Li, H. Liu, W. Zhang, T. Aida, W.-B. Zhang, K. Yue and S. Z. D. Cheng, *Science*, 2015, **348**, 424-428.
27. X. Y. Feng, G. X. Liu, D. Guo, K. N. Lang, R. M. Zhang, J. H. Huang, Z. B. Su, Y. W. Li, M. J. Huang, T. Li and S. Z. D. Cheng, *ACS Macro Lett.*, 2019, **8**, 875-881.
28. K. K. Lachmayr, C. M. Wentz and L. R. Sita, *Angew. Chem. Int. Ed.*, 2020, **59**, 1521-1526.
29. J. M. Dubois, *Useful quasicrystals*, World Scientific, 2003.
30. W. Man, M. Megens, P. J. Steinhardt and P. M. Chaikin, *Nature*, 2005, **436**, 993-996.
31. C. Tschierske, *Journal of Materials Chemistry*, 2001, **11**, 2647-2671.
32. B. M. Rosen, C. J. Wilson, D. A. Wilson, M. Peterca, M. R. Imam and V. Percec, *Chem. Rev.*, 2009, **109**, 6275-6540.
33. E. Apartsin and A.-M. Caminade, *Chem. Eur. J.*, 2021, **27**, 17976-17998.
34. S. D. Hudson, H.-T. Jung, V. Percec, W.-D. Cho, G. Johansson, G. Ungar and V. S. K. Balagurusamy, *Science*, 1997, **278**, 449-452.
35. B. M. Rosen, M. Peterca, C. Huang, X. Zeng, G. Ungar and V. Percec, *Angew. Chem. Int. Ed.*, 2010, **49**, 7002-7005.
36. N. Huang, Q. Xiao, M. Peterca, X. Zeng and V. Percec, *Mol. Phys.*, 2021, **119**, e1902586.
37. X. B. Liu, R. M. Zhang, Y. Shao, L. G. Xu, G. R. He, J. H. Huang, Z. H. Guo, W. B. Zhang, W. Tang and K. Yue, *ACS Macro Lett.*, 2021, **10**, 844-850.
38. V. Percec, M. N. Holerca, S. Uchida, D. J. P. Yeardley and G. Ungar, *Biomacromolecules*, 2001, **2**, 729-740.
39. X. Yao, L. Cseh, X. Zeng, M. Xue, Y. Liu and G. Ungar, *Nanoscale Horiz.*, 2017, **2**, 43-49.
40. V. Percec, W.-D. Cho, G. Ungar and D. J. P. Yeardley, *Angew. Chem. Int. Ed.*, 2000, **39**, 1597-1602.
41. V. Percec, M. N. Holerca, S. Nummelin, J. J. Morrison, M. Glodde, J. Smidrkal, M. Peterca, B. M. Rosen, S. Uchida, V. S. Balagurusamy, M. J. Sienkowska and P. A. Heiney, *Chem. Eur. J.*, 2006, **12**, 6216-6241.
42. X. Y. Yan, Q. Y. Guo, Z. W. Lin, X. Y. Liu, J. Yuan, J. Wang, H. M. Wang, Y. C. Liu, Z. B. Su, T. Liu, J. H. Huang, R. M. Zhang, Y. C. Wang, M. J. Huang, W. Zhang and S. Z. D. Cheng, *Angew. Chem. Int. Ed.*, 2021, **60**, 2024-2029.
43. T. Jun, H. Park, S. Jeon, S. Jo, H. Ahn, W.-D. Jang, B. Lee and D. Y. Ryu, *J. Am. Chem. Soc.*, 2021, **143**, 17548-17556.
44. T. Li, A. J. Senesi and B. Lee, *Chem. Rev.*, 2016, **116**, 11128-11180.
45. B. Lee, I. Park, H. Park, C.-T. Lo, Chang, Taihyun, and R. E. Winans, *J. Appl. Crystallogr.*, 2007, **40**, 496-504.
46. L. Palatinus and G. Chapuis, *J. Appl. Crystallogr.*, 2007, **40**, 786-790.
47. M. N. Holerca, D. Sahoo, B. E. Partridge, M. Peterca, X. Zeng, G. Ungar and V. Percec, *J. Am. Chem. Soc.*, 2018, **140**, 16941-16947.
48. J. H. Huang, Z. B. Su, M. J. Huang, R. C. Zhang, J. Wang, X. Y. Feng, R. Zhang, R. M. Zhang, W. P. Shan, X. Y. Yan, Q. Y. Guo, T. Liu, Y. C. Liu, Y. P. Cui, X. P. Li, A. C. Shi and S. Z. D. Cheng, *Angew. Chem. Int. Ed.*, 2020, **59**, 18563-18571.
49. D. He, N. N. Ekere and L. Cai, *Phys. Rev. E*, 1999, **60**, 7098-7104.